Research Article Vol. 33, No. 25 / 15 Dec 2025 / *Optics Express* 52793

Optics EXPRESS

Accounting for pulse shaper nonlinearity in action-detected two-dimensional electronic spectroscopy

MUYI ZHANG,[1] **STEPHANIE E. SANDERS,**[2] **JULIAN LÜTTIG,**[1] **STEFAN MUELLER,**[3] **ALASTAIR T. GARDINER,**[4] **TOBIAS BRIXNER,**[3,6] **AND JENNIFER P. OGILVIE**[5,7]

[1] *Department of Physics, University of Michigan, 450 Church Street, Ann Arbor, MI 48109, USA*
[2] *Department of Chemistry, Colgate University, 13 Oak Drive, Hamilton, NY 13346, USA*
[3] *Institut für Physikalische und Theoretische Chemie, Julius-Maximilians-Universität Würzburg, Am Hubland, 97074 Würzburg, Germany*
[4] *Center Algatech, Institute of Microbiology, Czech Academy of Sciences, 37901 Třeboň, Czech Republic*
[5] *Department of Physics, University of Ottawa, 150 Louis-Pasteur Pvt., Ottawa, ON K1N 6N5, Canada*
[6] *tobias.brixner@uni-wuerzburg.de*
[7] *jogilvi3@uottawa.ca*

Abstract: Pulse shapers are widely utilized in two-dimensional (2D) spectroscopy to generate a pump pulse pair with variable time delay and relative carrier–envelope phase. Their use in action-detected 2D spectroscopy has recently garnered interest due to the compatibility with microscopy and potentially higher sensitivity down to the single-molecule level. However, under the conditions necessary for action-detected 2D spectroscopy experiments, pulse shapers are prone to exhibiting nonlinear responses, obscuring the molecular response. Here, we illustrate the potential sources of nonlinearity in an acousto-optic programmable dispersive filter (AOPDF) and demonstrate methods to account for them in data collection and processing, enabling artifact-free action-detected 2D spectroscopy measurements.

1. Introduction

Multidimensional optical spectroscopy is widely used to study the energetic structure and ultrafast dynamics, such as energy transfer, in a wide range of solid-state, condensed-phase and gas-phase systems [1–3]. In two-dimensional (2D) spectroscopy, the correlation between excitation and detection frequency is measured using a sequence of laser pulses. Typically, the excitation axis is resolved via Fourier transformation of the time delay between the first two pulses (t_1 delay), which optimizes the time- and frequency-resolution trade off [1], whereas the detection axis is directly measured with a spectrometer. The use of a Fourier transformation to resolve the excitation axis in 2D spectroscopy requires a phase-stable pulse pair with better than $\lambda/100$ interferometric precision [1]. Multiple methods for scanning the t_1 delay in 2D spectroscopy have been implemented, such as with beam splitters and delay stages [4–9], wedges or rotating cover slides [10–13], or birefringent wedges [14]. To ensure phase stability, many of the aforementioned methods employ passive (*e.g.,* diffractive optics, common optics) or active (*e.g.,* interferometric tracking) phase stabilization.

Pulse shapers have emerged as an attractive tool for creating pulse pairs in both the visible and infrared regimes due to the inherent phase stability and high degree of phase control that they provide. The use of pulse shaping for multipulse optical spectroscopy measurements analogous to NMR was discussed by Warren and Zewail [15], and subsequently applied to 2D spectroscopy. The two most common pulse shaping methods are in the 4f geometry with a liquid-crystal [16] or acousto-optic [17] modulator at the Fourier plane or with an acousto-optic programmable

#580416 https://doi.org/10.1364/OE.580416
Journal © 2025 Received 30 Sep 2025; revised 5 Nov 2025; accepted 5 Nov 2025; published 8 Dec 2025

dispersive filter (AOPDF) [18]. Both 4*f* [19,20] and AOPDF [21–23] pulse shapers have been used in 2D electronic and vibrational spectroscopy. Pulse shapers based on acousto-optic modulators have the advantage of faster update rates compared to liquid-crystal-based pulse shapers, often enabling shot-to-shot pulse shaping [21,24]. In addition to being able to create pulse pairs with varying time delay, pulse shapers also offer control over the relative carrier–envelope phase (CEP) and higher-order phase terms. The control over the higher-order phase terms enables pulse compression to account for dispersion in the pulse shaper itself or other optical elements. The CEP control enables phase cycling of the pulses to suppress unwanted signals and isolate the nonlinear signals of interest [25]. Introducing a time-varying CEP allows the t_1 delays to be scanned in the partially or fully rotating frame [26]. This enables undersampling, which reduces the number of t_1 delays needed and thus the experiment time.

Action-detected (*e.g.,* fluorescence, photocurrent) 2D electronic spectroscopy (A-2DES) has recently gained interest as a complementary method to coherently detected 2D electronic spectroscopy (C-2DES) due to the potential sensitivity and ability to easily separate signals in the collinear geometry, which is compatible with microscopy. In A-2DES, a fourth pulse projects the coherent signal onto a population in an excited state that can be read out via an observable, such as fluorescence [27–31], photocurrent [32–34], photoelectrons/ions [35,36]. The addition of the fourth pulse also introduces a second excited-state absorption (ESA) pathway that can complicate the interpretation of action-detected 2D spectra [37,38]. Given the utility of pulse shapers in C-2DES, they have also been used to generate all four pulses for A-2DES. Fluorescence-detected 2DES (F-2DES) was first demonstrated by the Warren group [39]. Since then, pulse shapers have been employed for A-2DES by multiple groups using the detection of fluorescence [27–29,40], photoelectrons [35], photocurrent [41,42], and mass spectrometry [43]. Additionally, pulse shapers have been utilized to generate pulse trains for collinear C-2DES and higher-order (*i.e.*, higher than fourth order) nonlinear spectroscopy [44–48].

Both the new modes of detection and the increasing demands on the pulse shaper imposed by A-2DES motivate the investigation of potential artifacts and unwanted signals. It has been shown that incoherent mixing between linear responses can occur in A-2DES from a wide range of processes including exciton–exciton annihilation, Auger recombination, or nonlinearities in the detector [49–52]. Distinct from incoherent mixing which occurs during the detection period, an important potential source of artifacts in A-2DES that has had limited discussion in the literature is the nonlinearity associated with the use of pulse shapers to create the laser pulse sequence. The effect of artifacts from LCD-based pulse shapers on A-2DES has been addressed by realizing a complete and automated spectral interferometry characterization of all pulses during all scanning steps [53]. Here, we focus on providing a detailed discussion of the pulse shaper nonlinearities for AOPDF pulse shapers, which are widely used for A-2DES. Such nonlinearities can also impact C-2DES experiments employing AOPDF pulse shapers to generate the pump pulse pair, but to a lesser degree since a two-pulse sequence is generated instead of a four-pulse sequence. For example, the maximum time delay between pulses is typically a few hundred femtoseconds in traditional C-2DES using a pulse pair, in comparison with A-2DES experiments using a four-pulse sequence where multiple delays are scanned, often utilizing the full range of available delays of the pulse shaper. Generating fewer pulses also makes it easier to operate in the linear regime of the RF generator while maintaining sufficient pulse energies. Furthermore, the RF waveforms for creating four pulses are more complex and may therefore be more prone to nonlinearities. These nonlinearities in the context of AOPDF pulse shapers for A-2DES have been briefly discussed in a doctoral thesis [54] and in a few recent publications [55,56]. Recently, there was a detailed discussion of the RF nonlinearity in the context of higher-order infrared spectroscopy using a 4*f* acousto-optic pulse shaper [24]. Given the increasing interest in using pulse shapers for A-2DES, a detailed description of the nonlinearities and how to avoid or manage them is warranted.

Here, we will focus on RF-related nonlinearities present in an AOPDF pulse shaper with a TeO_2 crystal (Dazzler, Fastlite) in F-2DES using light harvesting complex II (LH2) and a molecular squaraine heterodimer (dSQAB3) [28] as example systems. We also propose two methods to account for the nonlinearities. These methods could be generalized to other pulse shapers (*e.g.*, AOPDFs with Ge or quartz crystals) and other action-detection methods. The exact regime exhibiting nonlinearity will depend on the pulse shaper, RF generator and wavelength range used. We discuss two main sources of nonlinearity that are important to avoid or to correct in A-2DES measurements. The first type of nonlinearity is the crystal-position-(*i.e.,* delay-)dependent diffraction efficiency caused by variations in the overlap between the acoustic and optical waves at different positions within the crystal. This is particularly important when measuring long time delays between the first and last pulse. We show how this can be corrected to minimize intensity variations as the maximum time between the pulses is increased (also discussed by Fastlite in the Dazzler manual). The second type of nonlinearity is the RF nonlinearity, which occurs due to nonlinearities in generating and amplifying the RF wave and in converting it into an acoustic wave. We characterize the RF nonlinearity using one-dimensional (time and frequency domain) as well as two-dimensional (time domain) measurements of the laser as a function of RF power, and numerical simulations of the two-dimensional signal. Finally, we discuss how and under what circumstances the RF nonlinearity can be corrected, illustrating the process for F-2DES measurements of LH2 and dSQAB3 with different RF powers.

2. Experimental setup

The experimental setups are described in detail in Supplement 1, and an overview of the experimental setups are shown in Fig. 1. Briefly, femtosecond laser pulses are spectrally broadened and partially compressed before being sent into the Dazzler. As seen in Fig. 1, all four pulses for the experiment are generated from a single input pulse by the Dazzler, which controls the relative time delays (t_1, t_2, t_3) and relative phases (φ_{12}, φ_{13}, φ_{14}) between pulses. We used a compatible RF amplifier (T4 generation, standard power or 50 W, Fastlite) to generate the acoustic pulses sent to the Dazzler to produce the pulse trains. Careful collimation of the beam after the pulse shaper is important to ensure pulse overlap between pulses generated over the entire crystal due to a small spatial walk-off introduced by diffraction at different positions in the crystal [57]. A variable, reflective neutral density wheel before the sample is used to adjust the power at the sample position as the RF power is changed. The pulses are then focused at the sample position. Laser-only measurements are performed by sending the laser beam directly into the avalanche photodiode (APD) [time domain] or the spectrometer [frequency domain], while fluorescence is collected in the 90° geometry on an APD, as illustrated at the bottom, right of Fig. 1.

For linear autocorrelation measurements, the time delay was scanned from –200 to 200 fs in steps of 0.25 fs in the lab frame, enabling higher-order signals to be resolved in the frequency domain. For the linear spectral interferometry, the time delay between the pulse pair was set to 200 fs. For the 2D measurements of the laser and LH2, t_1 and t_3 were both scanned from 0 to 91 fs in 7 fs steps in the partially rotating frame [58], *i.e.*, with a pulse-shaper reference frequency of $\omega_{\mathrm{ref}} = (1 - \gamma_0)\omega_0$, where ω_0 is the central frequency and $\gamma_0 = 0.11$. For the 2D measurements of dSQAB3, t_1 and t_3 were both scanned from 0 to 88 fs in 4 fs steps in the partially rotating frame with $\gamma_0 = 0.1$. To extract the rephasing and non-rephasing contributions, we employed a 27-fold phase cycling scheme [25,27,29]. The LH2 sample had a maximum OD of 0.26 (1 mm path length) and the dSQAB3 had a maximum OD of 0.35 (0.2 mm path length). The LH2 and dSQAB3 samples were flowed with a peristaltic pump and a micro annular gear pump, respectively, to prevent photobleaching. The total pulse energy was kept constant at 6 nJ for the measurements of LH2 regardless of the RF power used to generate the pulse trains in the pulse shaper with a variable ND filter. For the dSQAB3 measurements, the pulse

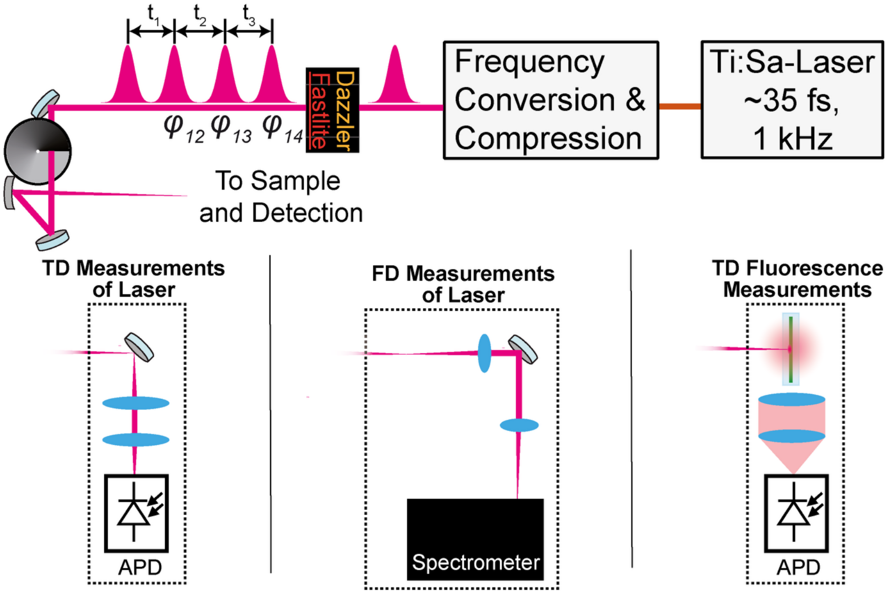

Fig. 1. Overview of the experimental setup (top) and detection schemes for the different measurements (bottom).

energy was 17 nJ when RF = 0.005, and 120 nJ when RF = 0.05 or 0.2. For the fluorescence measurements, long-pass filters were used to ensure spectral separation of the fluorescence from potential scattering of the laser. Reflective ND filters were used to guarantee that the signal on the detectors (APD or CCD) was in the linear regime of the corresponding detector.

3. Characterizing and accounting for nonlinearities

Acousto-optic pulse shapers are used to produce four individual pulses with specific time delays and phases from one input pulse [Fig. 2(a)]. The existence of nonlinearities in acousto-optic pulse shapers is well known [24,54,55,59–62]. As illustrated in Fig. 2(b), there is a saturation of the amount of light diffracted (pulse energy) versus the RF power used to generate the acoustic pulses due to the RF saturation. Only for low RF powers is the response linear, *i.e.,* nonlinearity is negligible. The development of new experiments, such as A-2DES, introduces new requirements for RF pulse shapes and powers, warranting the characterization and correction of nonlinearities as they pertain to the new experimental parameters.

3.1. Crystal-position-dependent diffraction efficiency

AOPDF pulse shapers utilize birefringent crystals to vary the amplitude, time delay and phase of the output pulses [63]. Within the AOPDF pulse shaper, a time-dependent acoustic wave is launched by a transducer driven by an RF generator. The traveling, acoustic wave propagates along the z-axis, producing a spatially dependent grating with the temporal shape of the RF signal. The incident optical pulse, also propagating along the z-axis, experiences z-dependent diffraction from the acoustic grating, such that the different frequency components of the pulse are diffracted efficiently at crystal positions where the phase-matching condition is met. The polarization of the diffracted wave is perpendicular to that of the input wave. Therefore, the position in the birefringent crystal at which the diffraction occurs determines the absolute group delay of the various frequency components of the diffracted pulse [63]. In AOPDF pulse shapers, there are variations in the diffraction efficiency as a function of position in the crystal due to

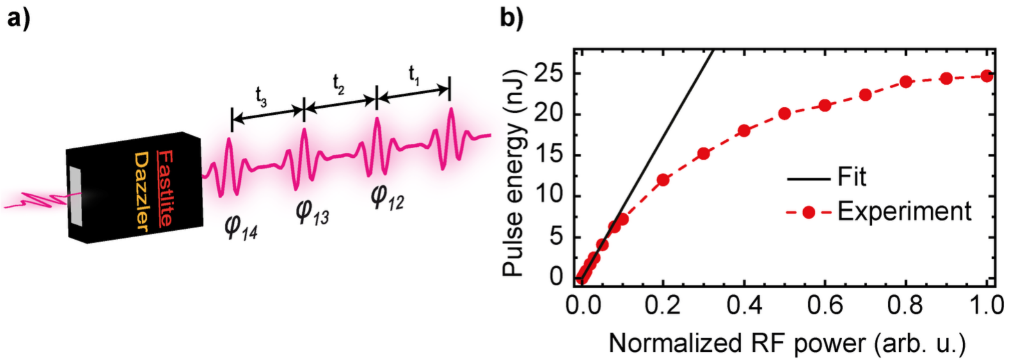

Fig. 2. Characteristics of an AOPDF pulse shaper like the Dazzler. (a) Principle of an AOPDF pulse shaper as it is used for A-2DES: generating a four-pulse sequence with variable delays and variable relative phases from a single input pulse. (b) The normalized RF power vs measured pulse energy shows a clear saturation effect. The linear fit was performed on the lower seven RF powers measured and represents the expected pulse energy in the absence of nonlinearity.

the complex diffraction pattern of the acoustic beam in the crystal. Analogous variations in diffraction efficiency are observed in 4*f* pulse shapers as a function of aperture position [64]. The Dazzler was designed to minimize this, but careful alignment is required especially when utilizing the full extent of the crystal. The location of the Dazzler aperture with respect to the beam was adjusted to ensure that the same spectral bandwidth was transmitted in three positions across the crystal (near the front, near the middle, near the end) and the intensity variations were minimized. The total maximum delay between the first and last pulse is significantly larger when scanning t_1, t_2, and t_3 with a pulse shaper for A-2DES compared to when only scanning t_1 for C-2DES, since conventionally t_2 is scanned with a delay stage and the Fourier transformation of t_3 is measured with a spectrometer. When the maximum time delay scanned in an experiment is only a few hundred femtoseconds, as is the case for C-2DES, the deviation is small. However, in A-2DES, it is desirable to scan time delays spanning the entire crystal to maximize the accessible waiting times, requiring all the pulses to have comparable intensity as t_1, t_2, and t_3 are varied. To characterize and correct for this diffraction efficiency variation, we measured the diffracted intensity of a single pulse from the Dazzler while varying the delay.

Briefly, we applied a short acoustic waveform (in time) with constant gain in 100 fs increments of absolute time delays across the crystal. The use of the constant gain mode ensures the peak RF power is conserved regardless of the phase settings of the RF wave. For the RF waveform inputs, we used a width of 30 nm and no applied 2^{nd}, 3^{rd}, and 4^{th} order phase, centered at 825 nm. This resulted in a relatively short acoustic waveform (as visualized in the Dazzler software) that still had a good amount of diffracted intensity for high signal-to-noise measurements. Then, we measured the diffracted intensity at each absolute time delay (*i.e.,* crystal position) on a spectrometer. The integrated signal from the spectrometer at each delay (normalized to the average diffracted intensity) is depicted as the green curve in Fig. 3(a). There is a large variation in the measured diffracted intensity as a function of delay (proportional to crystal position). Figure 3(b) illustrates how and where the diffraction occurs in the crystal, with the different opacities of the diffracted pulses representing the diffracted intensity. To correct for the crystal-position-dependent diffraction efficiency, the diffracted intensity must be scaled to yield a position-independent output intensity. A scaling factor is calculated based on the relative diffracted intensity. This scaling factor is used to apply a constant amplitude filter reducing the regions with high diffraction efficiency to match the lowest diffracted intensity. With the

Dazzler, this is done using the “ctimexxx.txt” (where “xxx” refers to the center wavelength of the Dazzler parameter set) file. A description for the “ctime” time correction is available as a pdf from Fastlite in the Dazzler manual. We describe the settings we used and how to calculate the scaling factor in Section 2 of Supplement 1. The results of this procedure are shown as purple in Fig. 3(a) and (c), where the variation of diffracted intensities is much smaller after correction. On the edges of the crystal, there is still some significant variation. However, the region of consistent diffracted intensity is much larger after the scaling factor is applied [Fig. 3(b) vs (c)], enabling a larger range of waiting times while maintaining constant pulse energy.

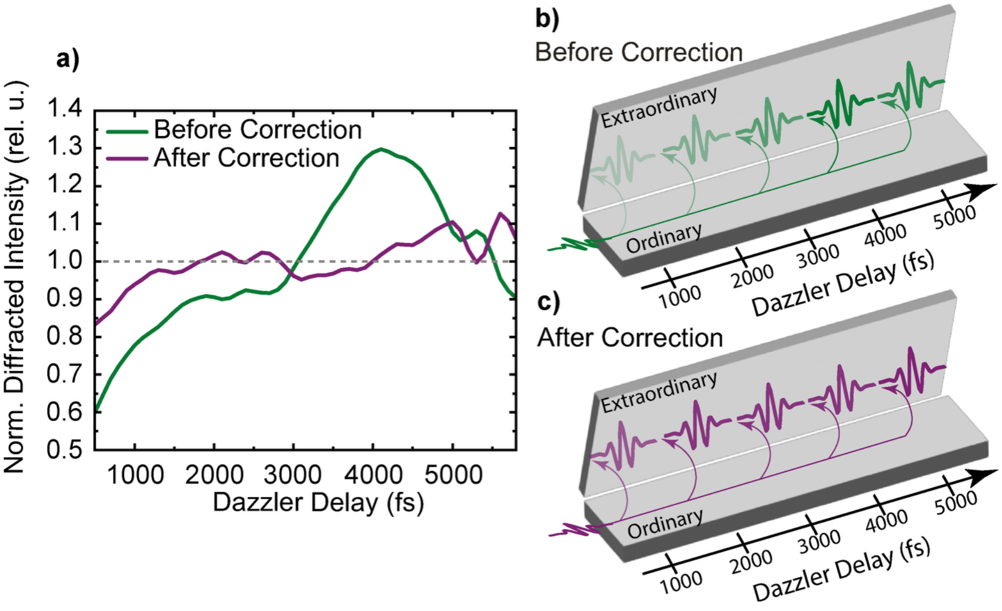

Fig. 3. Diffracted intensity of a single pulse from the Dazzler as a function of the Dazzler delay, which is proportional to the position where diffraction occurs in the crystal (a) and illustrations of the basic operation of an AOPDF pulse shaper with the crystal shown in gray with the ordinary and extraordinary axes and the optical pulses shown in green (b) and purple (c). When the optical wave diffracts from the acoustic grating at a given position in the crystal (*i.e.*, delay), the polarization flips. Before correction, there is a large variation in the diffracted intensity as seen in the graph (a, green curve) and the corresponding opacities of the diffracted pulses versus delays in the illustration of the acousto-optic crystal (b). After correction (a, purple curve and c), the diffracted intensity is fairly uniform with the largest deviations near the crystal edges.

The delay-dependent diffraction efficiency described above is only relevant to AOPDF pulse shapers and is not present in 4*f* pulse shapers in which the acoustic wave propagates perpendicular to the optical wave. Instead, 4*f* pulse shapers exhibit nonlinearity across the acousto-optic modulator, which must also be accounted for [24,59]. While delay-dependent diffraction intensity variations could result in spectral distortions and obscure any t_2 dependence of A-2DES spectra, the largest source of nonlinearity affecting the final 2D spectra stems from the RF generator. We refer to this nonlinearity as RF nonlinearity, which is dominated by the RF saturation, but also includes possible contributions from the conversion of the calculated wave to the generated wave, and the RF wave to the acoustic wave. Details of how to characterize and account for RF nonlinearities in the context of F-2DES measurements with the Dazzler will be discussed in the following sections.

3.2. Characterizing RF nonlinearity in linear measurements

The RF nonlinearity as a function of RF power can be easily visualized by collecting linear measurements of the laser-pulse train for different RF values while the signal level on the detector is kept constant (within linear operation of the detector). This enables determination of the linear regime of RF power for a given set of experimental conditions. Because the generated RF waveforms depend on the wavelength, bandwidth, and applied higher-order phases, the linear regime will differ slightly depending on the experimental settings. This characterization can be done in either time or frequency domain. Note that all RF power values given below are normalized to the maximum RF power.

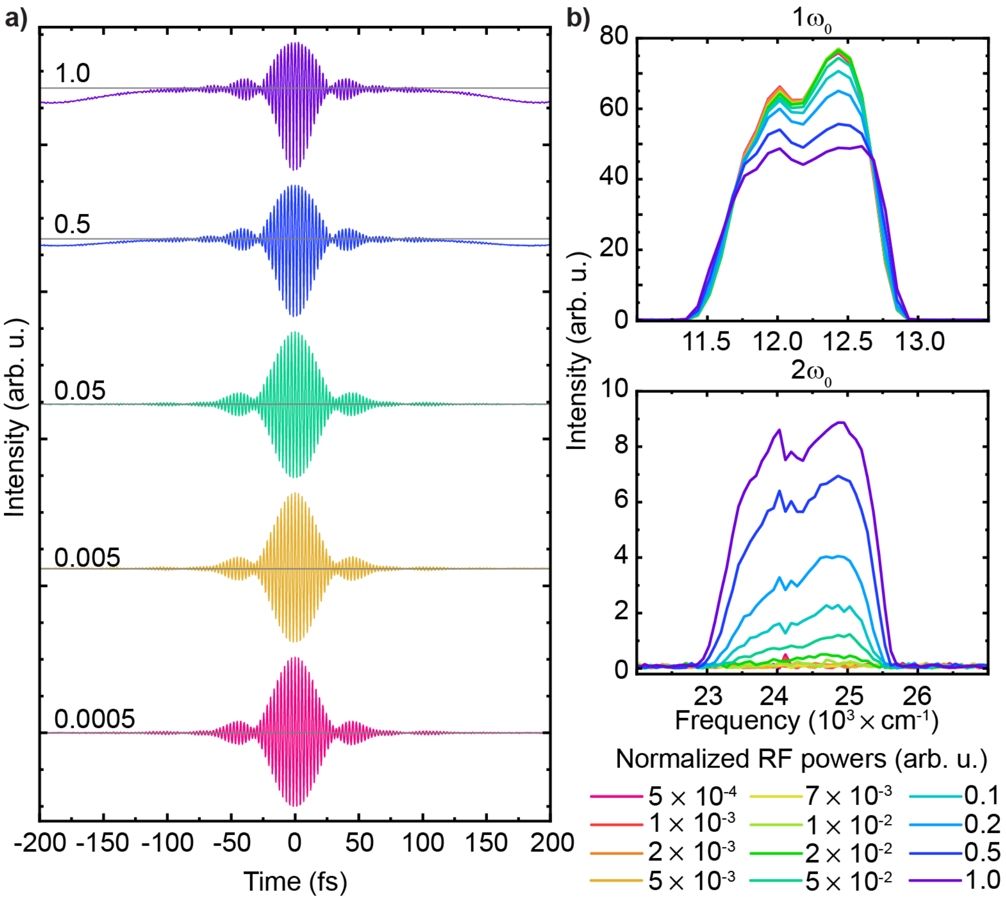

Fig. 4. Linear field autocorrelation of the four-pulse train where only t_2 is scanned ($t_1 = t_3 = 0$) for different normalized RF powers. (a) Linear autocorrelations for several normalized RF powers in the time domain. (b) Linear spectra from Fourier transformation of the linear autocorrelations for several RF powers around the central laser frequency ω_0 (top) and around $2\omega_0$ (bottom). Note that for RF powers less than 0.02, the $2\omega_0$ contribution is below the noise floor.

For the time-domain measurements, we measure the linear field autocorrelation of the four-pulse train where $t_1 = t_3 = 0$, while scanning t_2 in the lab frame. In this measurement, nonlinearity results in signals at harmonics above the fundamental frequency (ω_0) upon Fourier Transformation. We opted to perform the autocorrelation measurements with pulse trains consisting of four pulses to ensure that the RF pulses are as similar as possible to those used in the A-2DES measurements.

At $t_2 = 0$, the signal on the detector was kept constant for all RF powers with a variable ND filter to eliminate any possible differences due to detector nonlinearity. In the time domain, we can clearly observe increasing nonlinearity with higher RF power. For low RF powers the envelope of the linear autocorrelation is symmetric with respect to the average intensity values measured at long absolute delays as expected [Fig. 4(a), pink, gold, and green]. However the shape of the autocorrelation changes drastically for higher powers of 0.5 [Fig. 4(a), blue] and 1.0 [Fig. 4(a), purple], despite retaining the symmetry in time. Besides the asymmetry of the envelope of the main peak, we can even observe a deviation from the baseline for long delays. Since the applied waveform changes with the delay, the imprinted nonlinearity is a function of the delay. The effect of nonlinearity is easier to quantify in the frequency domain via Fourier transformation, as illustrated by Fig. 4(b). With increasing RF power, we first observe a change in amplitude of the linear spectrum at ω_0 while the spectral shape stays the same. When the RF power increases to 0.1 and above, the spectral shape is increasingly distorted. The amount of nonlinearity can be directly quantified by inspecting the higher harmonics of the linear autocorrelation. Even for RF powers as low as 0.05, which give an apparently intensity-symmetric autocorrelation envelope in the time domain [Fig. 4(a), green] and lead to a reduction in amplitude of the signal without any spectral distortions [Fig. 4(b)], a clear signal at $2\omega_0$ can be observed. The presence of any intensity above the noise floor at $2\omega_0$ in the linear autocorrelation is a clear indication of RF nonlinearity, which will lead to artifacts in A-2DES spectra. For very high RF powers (*e.g.*, 0.5 and 1.0), even higher harmonic signals at $3\omega_0$ and $4\omega_0$ appear, as illustrated in Fig. S1 Supplement 1, showing the high degree of nonlinearity for such RF values. It is important to note that the linear regime is not a fixed range, but will vary depending on wavelength, bandwidth, and applied phase. Therefore, it is important to characterize the linear regime whenever the input parameters are changed. The measurements in Fig. 4 are meant to illustrate how to easily identify the linear regime.

The measurements in Fig. 4 clearly demonstrate that the RF nonlinearity manifests itself when only one time delay is scanned. This is also important for the case of C-2DES employing a pulse shaper in the pump–probe geometry. In this setting, an AOPDF (or another pulse shaper) is inserted into the excitation beam of an ordinary pump–probe setup. The pulse shaper is then used to generate a pulse pair with variable delay, which is a relatively simple way to transform a pump–probe setup into a coherently detected 2D setup [19]. To characterize the conditions for generation of the pulse pair in the linear regime even further, we measured the spectral interference of a pulse pair with a delay of 200 fs via a CCD for different RF powers as C-2DES is typically measured in the frequency domain. We ensured that the intensity on the detector was constant by using a variable neutral density filter to eliminate any effect of detector nonlinearity in the same way as for the autocorrelation measurements discussed above. As expected, the spectrum of the pulse pair consists of several fringes [Fig. 5(a)] with the spacing corresponding to the 200-fs time delay between the pulses. The pronounced fringe contrast reflects the high degree of phase stability and beam overlap. For different RF powers, a change in the fringe intensity is visible, particularly at the edges of the spectrum. This is consistent with the spectral deviations observed in Fig. 4(b) from the autocorrelation of the pulse trains. Upon Fourier transformation into the time domain and taking the positive half of the time axis, the largest peak is at 200 fs, corresponding to the set time delay between the pulses. Note that the smaller peaks left and right of the main peak at 200 fs are caused by the Fourier transformation since we are not applying any window function. The nonlinearity appears as peaks at multiples of 200 fs (*e.g.,* 400 fs, 600 fs, 800 fs) with higher RF powers.

It is worth emphasizing that the time-domain and frequency-domain measurements shown in Fig. 4 and Fig. 5 illustrate the same effect. In both cases, there are spectral variations when the RF power is increased to high values (>0.5) and a growing peak at $2\omega_0$ or $2t_2$. However, the time-domain measurement is more sensitive to nonlinearity. In Fig. 4(b), there is noticeable

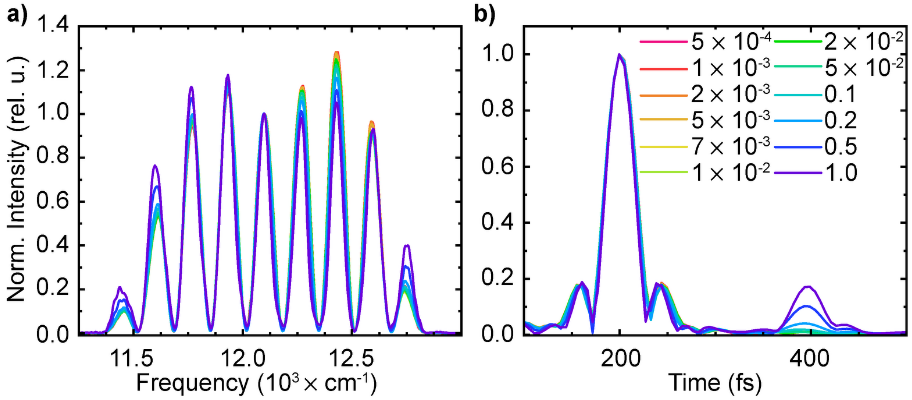

Fig. 5. Effect of nonlinearity for a four-pulse train with $t_2 = 200$ fs delay between pulses 2 and 3 ($t_1 = t_3 = 0$). (a) Spectral interferograms of the pulse train for different RF powers normalized to the central fringe to highlight spectral deviations. (b) Fourier transform of the results in (a) normalized to the intensity at the pulse delay (200 fs).

intensity at $2\omega_0$ for RF powers beginning at 0.02, while the first RF power with noticeable intensity at twice the delay between the pulses is 0.2 [in Fig. 5(b)].

3.3. Acousto-optic artifacts in F-2DES

In F-2DES, the signal is measured as a function of time delays (t_1, t_2, t_3) and relative phases (φ_{12}, φ_{13}, φ_{14}). Typically, 27-fold phase cycling, where $\varphi_{1x} = 0$, $2\pi/3$, or $4\pi/3$, is used to isolate the rephasing and non-rephasing signal contributions using weighted linear combinations [25,27,29]. Similar to the autocorrelations described in Section 3.2, the signal of the laser-pulse trains for F-2DES generated by the Dazzler can be measured to help quantify the artifacts occurring from the RF generation that can contaminate the 2D signal. This procedure was previously reported in the literature to quantify the contribution of the nonlinear artifact to the nonlinear signal of a sample response [55]. For our experiments, the signal level on the detector was attenuated with a variable ND filter to the same intensity used in the linear autocorrelation experiments, ensuring the only possible source of nonlinearity to be the RF generator. After performing the weighted linear combinations of the 27 phase combinations, we recover the nonlinear artifact signals which have the same frequency and phase relationship as the rephasing and non-rephasing signals of interest. In the ideal case where nonlinear artifacts are absent, only noise is recovered. However, as explained in Section 3.4, and Section 8 of Supplement 1, nonlinear artifacts can survive the 27-fold phase cycling procedure, contaminating the nonlinear signal of the sample as illustrated in Fig. 6.

If we operate the RF generator in the linear regime (*e.g.*, 0.005), the nonlinear artifact signal is approximately zero and we observe only noise in the rephasing time-domain signal [Fig. 6(a), left]. As the RF power is increased into the nonlinear regime, there is a noticeable signal above the noise floor [Fig. 6(a), middle]. The artifact manifests itself as an elongated stripe along the diagonal of the rephasing time-domain map. The nonlinearity is strongest when $t_1 = t_3$, resulting in a large signal along the diagonal in the time domain as reported previously [55]. As the raw signals for all three RF powers shown in Fig. 6(a) were recorded with the same detector intensity, the differences in amplitude of the signal after the weighted linear combination directly report on the magnitude of the nonlinearity. Upon Fourier transformation into the frequency domain, there is a clear narrow peak along the diagonal in the rephasing spectrum [Fig. 6(b), middle and right] when the RF power is in the nonlinear regime. At the lowest RF powers only a small peak along

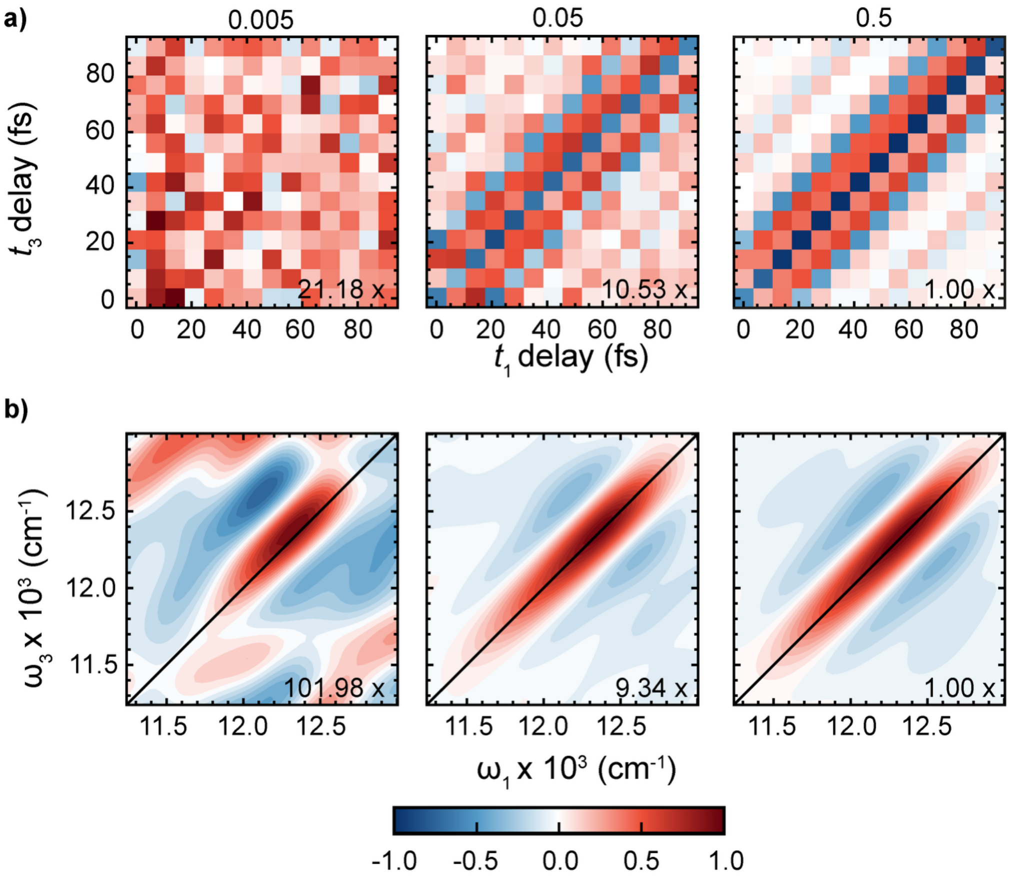

Fig. 6. Nonlinear artifact that contaminates the rephasing spectrum (real part) for RF powers of 0.005 (left), 0.05 (middle), and 0.5 (right) at $t_2 = 0$. (a) Time-domain maps. (b) Spectra in the frequency domain. Note that the spectrum for the lowest RF power is scaled by 101.98 so the observed features are predominantly noise.

the diagonal is present [Fig. 6(b), left]. We note that this data has been scaled by ~100× so this residual is typically smaller than the nonlinear response of the sample. It is also not symmetric along the diagonal like the signal for higher RF powers [Fig. 6(b), middle and right] confirming any nonlinearity for the lowest RF power is at the noise floor. There is also an artifact in the non-rephasing spectrum, as illustrated in Fig. S2 Supplement 1, but the nonlinearity is more significant in the rephasing spectrum, as we will explain further below. It is also worth noting that this artifact is present regardless of t_2, as seen by the similar time-domain rephasing plots at a t_2 delay of 500 fs in Fig. S3, Supplement 1.

The presence of these artifacts interferes with the signal of interest, changing the peak amplitudes and shapes, when measuring F-2DES spectra. To illustrate the effect of the RF nonlinearity on F-2DES spectra, we measured the light-harvesting complex II (LH2) of *Rhodoblastus acidophilus* with the same three RF powers used to measure the nonlinear artifact signal in Fig. 6. The absorptive F-2DES spectra for the three different RF powers and two different waiting times are shown in Fig. 7. We also show the rephasing and non-rephasing spectra for the same RF powers in the time and frequency domain for $t_2 = 0$ fs in Fig. S4 and S5 Supplement 1, respectively. For the lowest RF power (0.005), the RF nonlinearity is insignificant, as shown in the direct measurement of the pulse train with the same experimental settings in Fig. 6(b, left) being below the noise floor. Therefore, the observed spectral response originates fully from the sample. As seen in Fig. 7, left column, the F-2DES spectrum of LH2 consists of the two diagonal peaks for the B800 and B850 bands and two cross peaks. The diagonal peaks are quite round, while the cross peaks have comparable amplitude to each other and are of the same order of magnitude as the diagonal peaks. The RF nonlinearity artifact is elongated along the diagonal (Fig. 6) so this would stretch the lineshape of the diagonal peaks along the diagonal if it was significant. This spectrum is also in good agreement with previous F-2DES measurements of LH2 using a phase-modulated experimental setup that is not susceptible to the RF nonlinearity. One can refer to references [32,65,66] or Fig. S11 of Supplement 1 for verification. From the laser measurements, we know there is some nonlinearity for the medium RF power (0.05) and that the nonlinearity is mainly present along the diagonal in frequency space. This results in the elongation of the peaks in the F-2DES spectrum in Fig. 7 (middle column). Additionally, the ratio of the diagonal to cross peak intensity increases due to the addition of the artifact intensity on the diagonal. However, the general spectral features and frequencies are still identifiable under the medium RF power (0.05) conditions. Once the RF power is increased into the highly nonlinear regime (*e.g.,* 0.5), the F-2DES spectrum is dominated by the artifact, leading to elongated diagonal features and a complete suppression of the cross peaks. The same trend is visible for the rephasing and less pronounced for the non-rephasing spectral contributions, which are shown in Supplement 1 (Fig. S4 and Fig. S5). While using high RF powers leads to obvious artifacts, the identification of the artifact contribution is much more difficult in the medium regime (0.05) where the artifact leads to slight distortions of the lineshapes that may easily be misinterpreted. For example, at later waiting times ($t_2 = 500$ fs) the 2D spectra are slightly skewed above the diagonal. However, this change in spectral shape does not occur from a molecular response. Measuring the nonlinear artifact signal directly, as in Fig. 6, provides an easy handle for determining the presence of RF nonlinearity at a given RF power.

Ideally, all F-2DES experiments would be performed in the linear regime with low RF powers. As illustrated here, the excitation power needed for high signal-to-noise ratio (SNR) F-2DES data of LH2 is low enough that RF powers in the linear regime are more than sufficient. However, depending on the required experimental conditions for a given sample and the maximum diffracted power from the Dazzler, which depends highly on the second-order dispersion and alignment, achieving the desired SNR while operating in the linear regime may not be possible. For medium RF powers (*e.g.,* 0.05), where the nonlinearity is relatively small, it is still possible to identify molecular information from F-2DES spectra. However, care needs to be taken when considering lineshapes and relative peak amplitudes at a given t_2 because the presence of the RF nonlinearity artifact will distort the spectrum. Thus, it is desirable to remove the artifact, especially when higher RF powers are needed to achieve suitable SNR. We discuss two approaches that correct the artifact in Sections 3.5 and 3.6.

3.4. Modeling and simulating artifacts in F-2DES

To develop procedures for artifact correction, we first aim to find a suitable description of the observed artifact. The ideal spectral electric field of a four-pulse sequence with the parameters $\mathbf{t} = (t_0, t_1, t_2, t_3)$ and $\boldsymbol{\varphi} = (\varphi_1, \varphi_2, \varphi_3, \varphi_4)$ can be expressed as

$$\begin{aligned} E(\omega,\ \mathbf{t}, \boldsymbol{\varphi}) = {} & A(\omega)e^{-i\{\varphi_1+[\omega-\omega_0(1-\gamma_0)]t_0\}} + A(\omega)e^{-i\{\varphi_2+[\omega-\omega_0(1-\gamma_0)](t_0+t_1)\}} \\ & + A(\omega)e^{-i\{\varphi_3+[\omega-\omega_0(1-\gamma_0)](t_0+t_1+t_2)\}} + A(\omega)e^{-i\{\varphi_4+[\omega-\omega_0(1-\gamma_0)](t_0+t_1+t_2+t_3)\}}, \end{aligned} \tag{1}$$

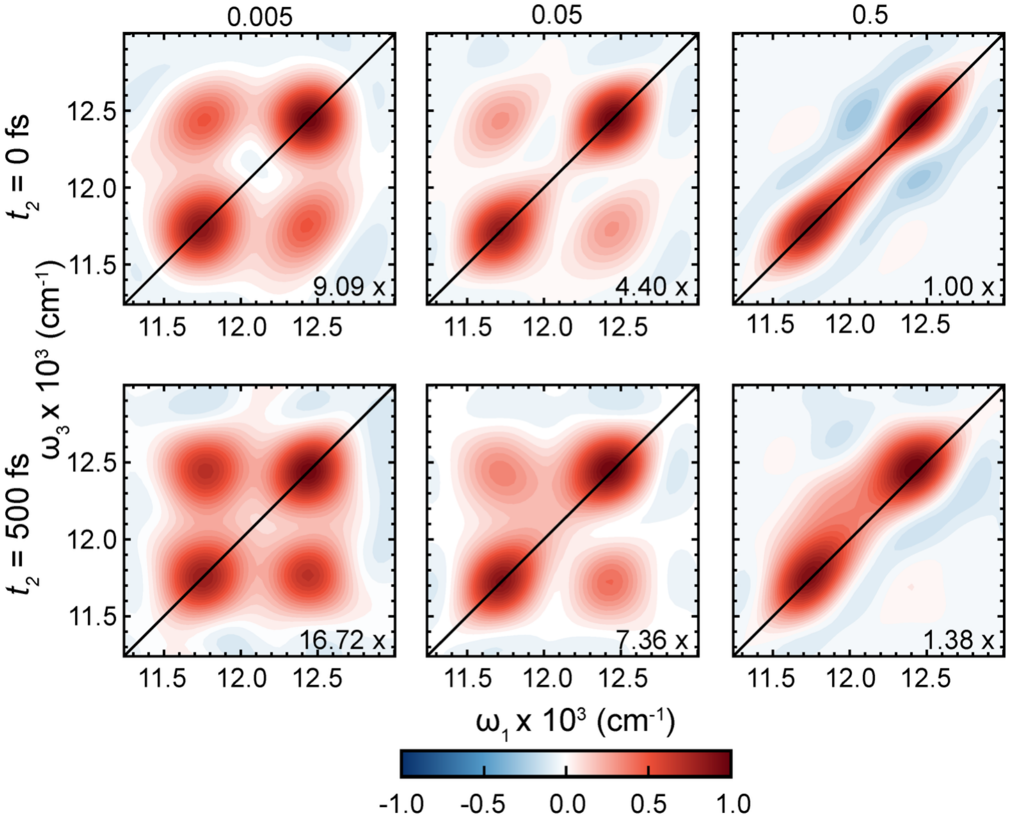

Fig. 7. Absorptive 2D spectrum of LH2 for three different RF powers of 0.005 (left), 0.05 (middle), and 0.5 (right). The top row displays the spectra for $t_2 = 0$ fs while the bottom row shows spectra for $t_2 = 500$ fs.

where γ_0 is the rotating frame parameter, t_0 is the temporal offset which is assumed to be zero in the following, and $A(\omega)$ is a Gaussian envelope with spectral width σ,

$$A(\omega) = \exp\left(-\frac{(\omega-\omega_0)^2}{2\sigma^2}\right), \tag{2}$$

which is normalized to its maximum absolute value, rendering all fields dimensionless in the simulation. The Dazzler artifact can be phenomenologically described as a spectral nonlinearity which results from distortions of the acoustic wave caused at high RF powers. In contrast to genuine optical nonlinearities resulting from material polarization and which are local in time (as is the case for, *e.g.*, second-harmonic generation), the artifact produced by the Dazzler arises locally in frequency because during the shaping process, each frequency is diffracted at a different location in the Dazzler crystal. If the Dazzler is operated in the nonlinear regime, the emitted spectral laser fields can thus be expanded as

$$E_{\mathrm{nonlin}}(\omega,\ \mathbf{t},\boldsymbol{\varphi}) \approx E(\omega,\ \mathbf{t},\boldsymbol{\varphi}) + \alpha E^2(\omega,\ \mathbf{t},\boldsymbol{\varphi}) + \beta E^3(\omega,\ \mathbf{t},\boldsymbol{\varphi}) + \ldots, \tag{3}$$

with second-order and third-order terms scaled by the dimensionless quantities α and β, respectively, which correspond to nonlinear pulse-shaper behavior. This spectral nonlinearity is especially problematic in the case of multi-pulse sequences as a multitude of unwanted higher-order electric field terms are generated. According to experimental observations (comparing

Fig. S5 with Fig. S8 of Supplement 1), the quadratic term in Eq. (3) is dominant and thus we set $\beta = 0$ in the following. To illustrate the impact of this nonlinearity, we calculate the intensity as it would be detected on a photodiode by spectrally integrating the absolute magnitude of the squared amplitude of $E_{\mathrm{nonlin}}(\omega,\ \mathbf{t}, \boldsymbol{\varphi})$, considering terms up to second order in α,

$$\begin{aligned} S_{\mathrm{nonlin}}(\mathbf{t}, \boldsymbol{\varphi}) &= \int |E_{\mathrm{nonlin}}(\omega,\ \mathbf{t}, \boldsymbol{\varphi})|^2 \mathrm{d}\omega. \\ &= \int \{ |E(\omega,\ \mathbf{t}, \boldsymbol{\varphi})|^2 + \alpha [E^2(\omega,\ \mathbf{t}, \boldsymbol{\varphi}) E^*(\omega,\ \mathbf{t}, \boldsymbol{\varphi}) \qquad , \\ &+\ E(\omega,\ \mathbf{t}, \boldsymbol{\varphi})(E^*(\omega,\ \mathbf{t}, \boldsymbol{\varphi}))^2] + \alpha^2 |E(\omega,\ \mathbf{t}, \boldsymbol{\varphi})|^4 \}\ \mathrm{d}\omega + O(\alpha^3) \end{aligned} \tag{4}$$

where we sample $\boldsymbol{\varphi}$ corresponding to a 27-fold ($1 \times 3 \times 3 \times 3$) phase-cycling scheme to resolve individual fourth-order [in $E(\omega,\ \mathbf{t}, \boldsymbol{\varphi})$] nonlinear signal contributions. We then extract the rephasing (R) and non-rephasing (NR) nonlinear signal contributions of the artifact using [25]

$$S_{\mathrm{ar,R}}(\mathbf{t}) = \frac{1}{27} \sum_{n=0}^{2} \sum_{m=0}^{2} \sum_{l=0}^{2} S_{\mathrm{nonlin}}(\mathbf{t}, \boldsymbol{\varphi}) e^{-il\Delta\varphi_{21}} e^{-im\Delta\varphi_{31}} e^{in\Delta\varphi_{41}}, \tag{5}$$

$$S_{\mathrm{ar,NR}}(\mathbf{t}) = \frac{1}{27} \sum_{n=0}^{2} \sum_{m=0}^{2} \sum_{l=0}^{2} S_{\mathrm{nonlin}}(\mathbf{t}, \boldsymbol{\varphi}) e^{il\Delta\varphi_{21}} e^{-im\Delta\varphi_{31}} e^{in\Delta\varphi_{41}}, \tag{6}$$

with the phase increments $\Delta\varphi_{21} = \Delta\varphi_{31} = \Delta\varphi_{41} = 2\pi/3$. Figures 8(a) and 8(b) show the simulated time-domain maps for the rephasing and the non-rephasing signal contributions of the artifact in the case of $\alpha = 1$. Note that in the absence of any nonlinearity, *i.e.*, $\alpha = 0$, Eqs. (5) and (6) do not yield any signals that survive the phase-cycling procedure, as expected for an ideal pulse shaper. If $\alpha > 0$, nonzero signals appear because the artifact represents a source of nonlinearity due to the self-modulation term $\alpha^2 |E(\omega,\ \mathbf{t}, \boldsymbol{\varphi})|^4$ which is generated by interference of nonlinear electric-field terms in Eq. (4). This self-modulation term carries the phase signatures of rephasing and non-rephasing signals and thus survives the phase-cycling procedure. We simulated the signals with a Gaussian spectral width of $\sigma = 50$ nm centered around 825 nm with a partially rotating frame parameter of $\gamma_0 = 0.11$ and varied t_1 and t_3 from –91 to 91 fs in 27 steps with $t_2 = 0$ fs. In the rephasing signal [Fig. 8(a)], the typical stripe is evident along the diagonal, as observed in Fig. 6(a) for higher RF powers. The stripe has a Gaussian cross section according to Eq. (2). The weak oscillatory behavior along the antidiagonal is caused by the partially rotating frame and displays an undersampled electric field oscillation. In the non-rephasing time-domain map, the artifact is antidiagonal due to the different phase signature which effectively changes the sign of t_1. As a result, the non-rephasing contribution of the artifact is less prominent than the rephasing contribution when only positive delays are scanned, which is how A-2DES experiments are typically performed. The positive delay section of the rephasing signal [red square in Fig. 8(a)] is extracted and shown in Fig. 8(b) together with the measurement of the laser intensity at RF = 0.05 (Fig. 6(a), middle, replotted in Fig. 8(b) for comparison). The good agreement between simulation and experiment confirms that the artifact predominantly originates from the second-order nonlinearity as employed in the simulation. The artifact is also present with a lower amplitude even for very small values of α, as shown in Fig. S8, Supplement 1.

We also carried out simulations with inclusion of the cubic term in Eq. (3). If higher-order electric-field terms are present, oblique lower-amplitude stripes appear due to additional cross-correlation contributions in both rephasing and non-rephasing time-domain maps [Fig. S8(c), Supplement 1]; however, the (off-)diagonal artifact is still dominant.

It is worth noting that the shape of the spectral amplitude $A(\omega)$, especially the bandwidth, as well as the rotating frame parameter γ_0 have an influence on the shape of the artifact. This causes the artifact to appear broader in the time-domain map in the case of a smaller spectral bandwidth. Note further that (non)linear chirp, when identical in all four pulses, does not affect the shape of the artifact, since such "global" phase terms vanish in Eq. (4).

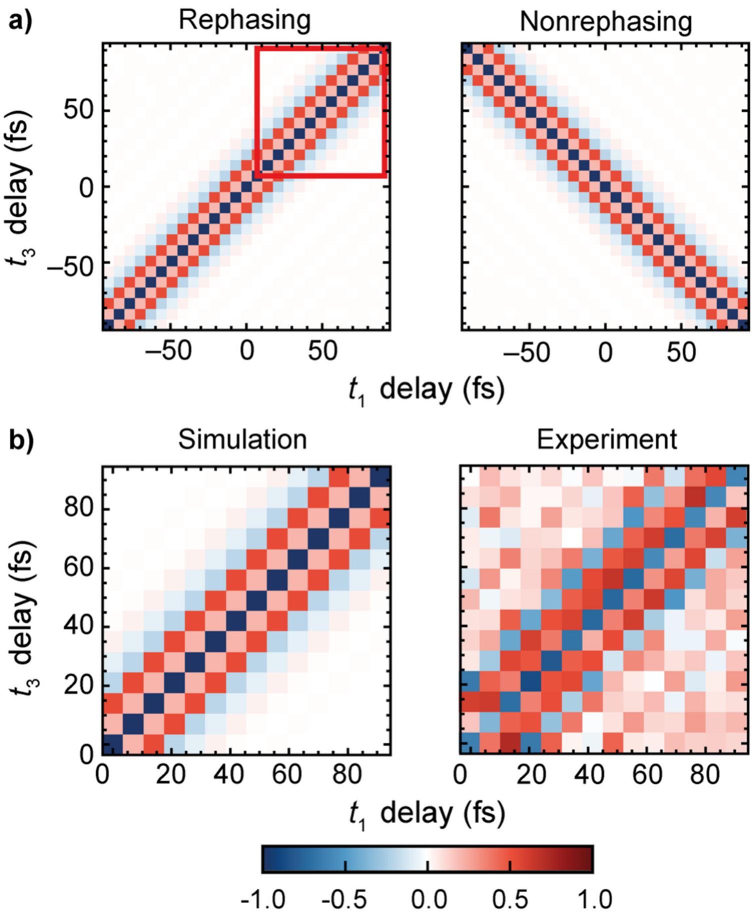

Fig. 8. Normalized time-domain maps of simulated Dazzler artifacts (real part). (a) Simulated rephasing and non-rephasing signal contributions in case of $\alpha = 1$. The simulation corresponds to the detection of the intensity of four-pulse sequences with scanned time delays and phases on a single-pixel detector after weighted linear combination. The artifact manifests as a strong diagonal stripe in the rephasing signal, whereas it is an antidiagonal stripe in the non-rephasing signal. (b) The close-up of the positive–positive quadrant marked in red in panel (a) is shown along with the experimental data at RF = 0.05 from Fig. 6(a), middle, plotted here again for comparison.

3.5. Artifact removal by amplitude scaling

To compensate for the acousto-optic nonlinearity of the pulse shaper, the spectral amplitude, and in turn the amplitude of the acoustic waveform, can be scaled by a “correction factor” as briefly discussed in literature [54]. Because the nonlinearity depends on the exact shape of the RF waveforms generated, the precise nonlinearity at a given RF power will be slightly different for every combination of time delays and phases. To calculate the correction factor, one first needs to measure the laser intensity as a function of all time delays and phases needed for the desired F-2DES experiment at a low RF power in the linear regime [*e.g.,* 0.005, $S_{\mathrm{lin}}(\mathbf{t}, \boldsymbol{\varphi})$] and at the desired RF power needed to reach the target SNR [*e.g.,* 0.05, $S_{\mathrm{nonlin}}(\mathbf{t}, \boldsymbol{\varphi})$]. Taking the ratio of the two measurements for every time and phase combination yields the correction factor

$$\zeta(\mathbf{t}, \boldsymbol{\varphi}) = \frac{S_{\mathrm{lin}}(\mathbf{t},\ \boldsymbol{\varphi})}{S_{\mathrm{nonlin}}(\mathbf{t}, \boldsymbol{\varphi})} = \frac{\int |E(\omega,\ \mathbf{t}, \boldsymbol{\varphi})|^2 \mathrm{d}\omega}{\int |E_{\mathrm{nonlin}}(\omega,\ \mathbf{t}, \boldsymbol{\varphi})|^2 \mathrm{d}\omega}, \tag{7}$$

where $S_{\mathrm{lin}}(\mathbf{t}, \boldsymbol{\varphi})$ and $S_{\mathrm{nonlin}}(\mathbf{t}, \boldsymbol{\varphi})$ are normalized to their respective maxima prior to calculating the ratio. Note that this correction factor needs to be recalculated any time the input spectrum to the Dazzler changes or a different set of time delays, phases or RF powers is used. The correction factor is then used as a scaling factor for each pulse shape when performing the measurement with the desired RF power,

$$P_{\mathrm{corr}}(\mathbf{t},\ \boldsymbol{\varphi}) = \zeta(\mathbf{t}, \boldsymbol{\varphi})\ P_{\mathrm{nonlin}}(\mathbf{t}, \boldsymbol{\varphi}), \tag{8}$$

where $P_{\mathrm{nonlin}}(\mathbf{t},\ \boldsymbol{\varphi})$ and $P_{\mathrm{corr}}(\mathbf{t},\ \boldsymbol{\varphi})$ refer to the RF powers of each pulse shape before and after correction, respectively. As the correction factors are based on measured laser intensities, deviations may occur due to the nontrivial relationship between measured optical intensity and applied RF power. For this reason, the correction factors have to be determined iteratively, *i.e.*, $S_{\mathrm{corr}}(\mathbf{t},\ \boldsymbol{\varphi})$ [the laser intensity measured at the desired RF power with $P_{\mathrm{corr}}(\mathbf{t},\ \boldsymbol{\varphi})$ applied] is measured and reinserted as a new $S_{\mathrm{nonlin}}(\mathbf{t}, \boldsymbol{\varphi})$ in Eq. (7) to receive a new set of $\zeta(\mathbf{t}, \boldsymbol{\varphi})$. The iterations repeat until the nonlinear artifact signals recovered from $S_{\mathrm{corr}}(\mathbf{t},\ \boldsymbol{\varphi})$ via phase-cycling exhibit no visible artifacts above the noise floor (i.e., that the rephasing 2D time-domain map resembles Fig. 6(a), left). The final correction factor is thus the product of all the intermediate correction factors for each iteration. The measurement of the sample is performed with the final correction applied. More details are discussed in Section 6 of Supplement 1.

As an illustration, we examine the absorptive F-2DES spectrum of the molecular dimer dSQAB3 at $t_2 = 30$ fs. Unlike LH2, dSQAB3 requires much higher excitation power to achieve good SNR, as illustrated by the noisy spectrum measured with low RF power in the linear regime [Fig. 9(b), 0.005 Reference]. With higher RF powers, the spectra exhibit significantly improved SNR, while suffering from more visible nonlinear artifacts [Fig. 9(a), 0.05 Uncorrected and 0.2 Uncorrected], elongating the diagonal peaks and, in the extreme case of RF = 0.2, even the cross peaks, along the diagonal. The aforementioned amplitude correction method largely removes these artifacts [Fig. 9(a), 0.05 Amp. and 0.2 Amp.].

It is worth emphasizing that the amplitude correction approach assumes that only the amplitude of the RF pulse is changing. Therefore, it is unlikely that the correction will work well for a laser source that exhibits substantial intensity or spectral fluctuations over the course of the measurements. In addition, the autocorrelation measurements of the laser shown in Fig. 4 demonstrate that there are spectral changes for very high RF powers. When the correction is attempted under such conditions, the final spectrum is overcorrected along the diagonal. This could possibly explain the extended hole in the middle of the spectrum of RF = 0.2 [Fig. 9(a), 0.2 Amp.] which is not visible in the low-power uncorrected measurement. By comparing the laser spectrum in the linear RF regime (*e.g.,* 0.005) to the laser spectrum with the desired RF power for the experiment, it is easy to confirm if only the amplitude is changing with increased RF power or if there are also spectral changes. This check makes it straightforward to determine whether this correction method will work.

3.6. Artifact removal by subtraction

The amplitude correction of the waveforms is a rather time-consuming procedure in view of several iterations of measurements needed to obtain suitable correction factors, and it also has certain limitations as discussed above. In the following, we show an alternative approach which can be carried out in a single measurement and that works well in the regime of medium RF powers that tend to exhibit artifacts.

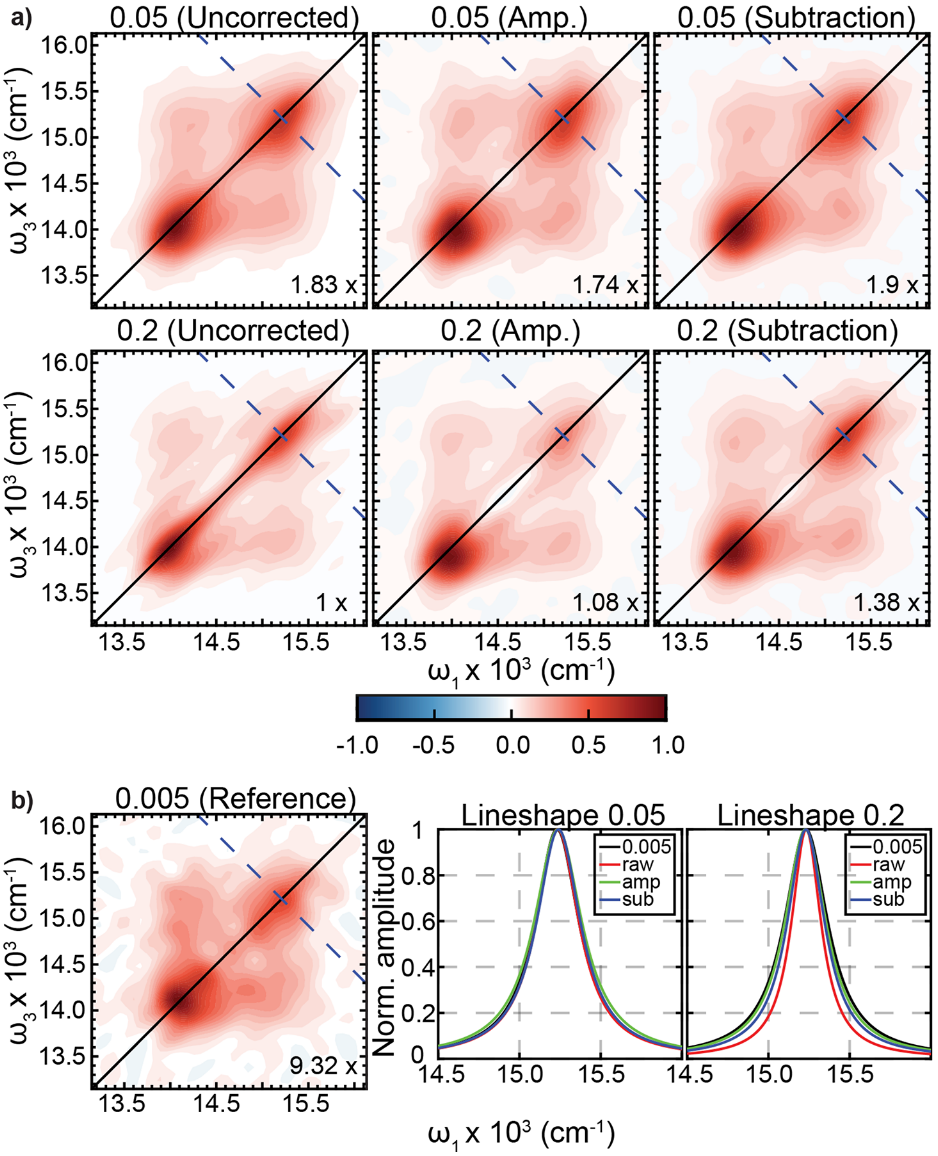

Fig. 9. Correction of the nonlinear artifact for molecular dimer dSQAB3 at t_2 = 30fs. (a) Comparison of the corrected and uncorrected absorptive 2D spectra measured at medium RF power (RF = 0.05, top row) and high RF power (RF = 0.2, bottom row). Uncorrected: Raw spectra without any correction. Amp.: Corrected spectra using the amplitude correction method as described in Section 3.5. Subtraction: Corrected spectra using the subtraction method as described in Section 3.6. (b) Left: Reference absorptive 2D spectrum at low RF power (RF = 0.005). Right: Comparison of the anti-diagonal lineshapes of the upper diagonal peaks (blue dashed lines in all the absorptive 2D spectra) fitted to a Lorentzian function. Medium and high RF powers are compared separately in two plots. Black curve labeled "0.005": Taken from the low RF power reference spectrum. Red curve labeled "raw": Taken from the uncorrected spectra. Green curve labeled "amp": Taken from the amplitude-corrected spectra. Blue curve labeled "sub": Taken from the artifact-subtracted spectra. Note that all the absorptive 2D spectra are normalized to the maxima of the uncorrected spectrum at RF = 0.2, with the scaling factors indicated on the bottom right of each spectrum.

In general, the occurrence of the artifact in F-2DES experiments implies that the artifact-associated components of the pulse sequences contributed to the sample response, resulting in an artifact-contaminated fluorescence signal. These contaminations persist even after applying the phase-cycling procedure. To describe this situation using response functions and to avoid the complexity of convolution integrals in the time domain, we adopt a simplified frequency-domain description of the signal. In this approximation, the total artifact-contaminated fluorescence signal $F_{\mathrm{tot}}(\omega)$ is expressed as a sum of contributions involving different powers of the artifact-affected electric field $E_{\mathrm{nonlin}}(\omega)$. In particular, considering up to the fourth power of $E_{\mathrm{nonlin}}(\omega)$ and ignoring higher-order terms, both the fourth and the second power of $E_{\mathrm{nonlin}}(\omega)$ ($|E_{\mathrm{nonlin}}(\omega)|^4$ and $|E_{\mathrm{nonlin}}(\omega)|^2$) contribute to the fluorescence signal. Note that we explicitly include $|E_{\mathrm{nonlin}}(\omega)|^2$ because this quantity, due to the nonlinearity, contains field terms that have suitable phase patterns to generate fluorescence by a fourth-order process as well. By expanding $|E_{\mathrm{nonlin}}(\omega)|^4$ and $|E_{\mathrm{nonlin}}(\omega)|^2$ with an artifact-affected electric field up to second order as in Eq. (3), $E_{\mathrm{nonlin}}(\omega) = E(\omega) + \alpha E^2(\omega)$, we obtain various terms in different orders of $E(\omega)$. Given the fact that only terms with equal powers of E and E^*, *i.e.*, $E^m(E^*)^n$ with $m = n$ where $m \geq 2$ and $n \geq 2$, contribute terms with phase combinations of fourth-order signals that can be extracted by phase cycling, the total fluorescence signal can be expressed as

$$\begin{aligned} F_{\mathrm{tot}}(\omega) \approx\ & Q^{(4)}(\omega)E^2(\omega)(E^*(\omega))^2 + Q^{(4)}(\omega)\alpha^2E^2(\omega)(E^*(\omega))^2 \\ & + Q^{(6)}(\omega)4\alpha^2E^3(\omega)(E^*(\omega))^3 + Q^{(8)}(\omega)\alpha^4E^4(\omega)(E^*(\omega))^4, \end{aligned} \tag{9}$$

where all electric field terms scaled by α represent electric-field components that are associated with the artifact. In Eq. (9), $Q^{(n)}(\omega)$ represents the n-th order frequency-dependent response function. While the desired rephasing and non-rephasing fourth-order signals are represented by $Q^{(4)}(\omega)E^2(\omega)(E^*(\omega))^2$, the artifact-terms that scale with $E^2(\omega)(E^*(\omega))^2$, $E^3(\omega)(E^*(\omega))^3$ and $E^4(\omega)(E^*(\omega))^4$ also include field permutations with phase combinations that coincide with those of the desired fourth-order signals, as shown in Section 8 in the Supplement 1. In other words, the artifact represents a contamination that has the same phase signature as the desired fourth-order signals. In the case of weak artifact strength, only the term $\alpha^2E^2(\omega)(E^*(\omega))^2$ is significant and higher-order terms, both in α and E, can be neglected. Then, the total signal can be expressed as the sum of the "true" molecular signal $F_{\mathrm{sample}}(\omega)$ and an artifact signal $F_{\mathrm{ar}}(\omega)$:

$$F_{\mathrm{tot}}(\omega) = F_{\mathrm{sample}}(\omega) + F_{\mathrm{ar}}(\omega) \approx Q^{(4)}(\omega)E^2(\omega)(E^*(\omega))^2 + \alpha^2Q^{(4)}(\omega)E^2(\omega)(E^*(\omega))^2 . \tag{10}$$

Since $F_{\mathrm{ar}}(\omega)$ includes terms that share the same phase signatures as the desired signal contributions in $F_{\mathrm{sample}}(\omega)$, $F_{\mathrm{ar}}(\omega)$ cannot be removed by any means of phase cycling. However, we can make use of the measurement of the laser-pulse train, *i.e.*, Eq. (4), which provides the term $S_{\mathrm{ar}}(\omega) = \alpha^2|E(\omega)|^4$ that also survives phase cycling and contains information on the same field distortions as the artifact-affected term F_{ar} in the fluorescence signal. Thus, S_{ar} can be used as an approximate measure to subtract the artifact. To account for deviations between $F_{\mathrm{ar}}(\omega)$ and $S_{\mathrm{ar}}(\omega)$, we aim to find a scaling factor $\eta \approx Q^{(4)}(\omega)$ such that

$$F_{\mathrm{ar}}(\omega) \approx \eta S_{\mathrm{ar}}(\omega). \tag{11}$$

Then one can eliminate the artifact by simple subtraction,

$$F_{\mathrm{sample}}(\omega) \approx F_{\mathrm{tot}}(\omega) - \eta S_{\mathrm{ar}}(\omega). \tag{12}$$

In the following, we seek to perform the artifact correction with the experimental time-domain maps, where the artifact is more discernable from the molecular response. A subtraction with time-domain maps is a valid approach because, due to the linearity of the Fourier transformation, a subtraction performed in the frequency domain is equivalent to a subtraction in the time domain. While $S_{\mathrm{ar}}(\mathbf{t})$ can be obtained by measuring the laser intensities across the variation of all pulse-sequence parameters [Eq. (4)], the determination of the scaling factor η is not straightforward, as it must compensate for t_2-dependent variations arising from the sample response function $Q^{(4)}$, which effectively modulates the artifact amplitude in the fluorescence signal. To find suitable values for η, we aim to find $\eta(t_2)$ such that subtracting the scaled artifact signal from the total signal leaves only noise in a region of the real-valued rephasing time-domain map where sample coherences have decayed. In particular, we select a quadratic section of the time domain map ($t_1 \geq \tau$ and $t_3 \geq \tau$, where τ is a positive time after which the sample coherences have decayed) where only artifact signal is expected to remain. We perform this procedure for every t_2 delay by minimizing the variance of the residual:

$$\eta(t_2) = \underset{\eta \in \mathbb{R}}{\operatorname{argmin}}\{\mathrm{Var}[F_{\mathrm{tot,\,R}}(t_1 \geq \tau, t_3 \geq \tau) - \eta S_{\mathrm{ar,R}}(t_1 \geq \tau, t_3 \geq \tau)]\}. \tag{13}$$

The right column of Fig. 9(a) shows the corrected 2D spectra of dSQAB3 using the subtraction with the optimized $\eta(t_2)$ of Eq. (13). For $t_2 = 30$ fs, we have determined $\eta(30\ \mathrm{fs}) = 0.63$ at RF = 0.05 and $\eta(30\ \mathrm{fs}) = 0.92$ at RF = 0.2, where we used $\tau = 44$ fs. For both RF powers, the artifact can be corrected and the lineshape distortions are removed. We have also tried this approach on LH2 (see Supplement 1, Fig. S9 and S10). While the spectrum can be corrected for RF = 0.05, the correction is not possible at RF = 0.5. At such high RF powers, the higher-order terms $4Q^{(6)}(\omega)\alpha^2 E^3(\omega)(E^*(\omega))^3$ and $\alpha^4 Q^{(8)}(\omega)E^4(\omega)(E^*(\omega))^4$ in Eq. (9) as well as new terms generated by cubic electric-field terms in Eq. (3) become significant. Thus, the deviation between F_{ar} and S_{ar} increases in a nontrivial way which cannot be compensated by a scaling factor. Moreover, the artifact exhibits spectral distortions for which the subtraction cannot account for. Hence, the conditions for the subtraction are only satisfied in case of low artifact-contamination regimes. In principle, such artifact correction can be carried out "on-the-fly" by simultaneously measuring a part of the excitation beam used in the F-2DES experiment along with the fluorescence of the sample using two separate detectors. Such an approach saves acquisition time and minimizes correction errors due to laser stability drift.

Finally, we examine the anti-diagonal lineshapes of the upper diagonal peaks of the raw and corrected absorptive 2D spectra. For each 2D spectrum displayed in Fig. 9, we take an anti-diagonal line that crosses the center of the upper diagonal peak (blue dashed lines that intersect with the diagonal at 15210.3 cm^{-1}), retrieve the data and fit them to a Lorentzian function. The full width at half maximum of these fitted Lorentzian curves are reported in Table 1. As demonstrated in Fig. 9(b, Lineshape 0.05), the normalized Lorentzian fits are similar in shape for medium RF power when compared to the low RF power reference (black curve labeled "0.005"), indicating that the artifacts are not very strong and the extent of correction is minor. However, if uncorrected, the lineshape is considerably narrower for high RF power measurements (Lineshape 0.2, red curve labeled "raw") compared to the low RF power reference. Both correction methods improve the lineshapes for the high RF power measurements (green curve labeled "amp" and blue curve labeled "sub"). We note that Zhao et al. recently reported a related approach to correcting nonlinearities in their Dazzler-based F-2DES studies of quantum dots [67].

Table 1. Full width at half maximum of the Lorentzian anti-diagonal lineshapes in Fig. 9

RF power	0.005	0.05			0.2		
Correction	Reference	Raw	Amp	Sub	Raw	Amp	Sub
FWHM (cm^{-1})	328.46	319.83	359.02	328.44	221.43	308.84	279.60

4. Conclusion

We have discussed the effect of nonlinearity introduced by pulse shapers in action-detected two-dimensional (2D) spectroscopy. Here, we focused on fluorescence-detected 2D spectroscopy using an acousto-optic programmable dispersive filter (AOPDF). For higher radio-frequency (RF) powers, the optical output power does not scale linearly. This simple effect has a significant impact on action-detected 2D spectra. If a pulse pair is created, such as in the case of linear field autocorrelations, the nonlinearity can lead to spectral distortions of the retrieved spectrum for high RF powers. The nonlinearity manifests itself in signal contributions at the harmonics of the central frequency. The range of RF powers that exhibit nonlinearity depends significantly on the wavelength, bandwidth and applied phase. Therefore, it is critical to characterize the linear RF regime for the specific experimental parameters of a given experiment. The nonlinear artifacts are most significant when a four-pulse sequence is generated with a single AOPDF, such as in the context of action-detected 2D spectroscopy. The nonlinearity results in a large artifact on the diagonal in the 2D spectra. Recognizing the characteristics of the artifact can help differentiate it from molecular responses. The artifact can distort the lineshape significantly as we have demonstrated in the case of one of the antenna complexes of purple bacteria (LH2) and a molecular dimer (dSQAB3). Performing measurements on the laser pulses directly and RF-power-dependent measurements can also help differentiate the artifact from the molecular response.

The extent to which the nonlinear artifact needs to be suppressed relative to the molecular signal depends on the specific experimental investigation. In order to investigate lineshapes, the nonlinearity needs to be below the noise floor requiring low RF powers. However, if the focus of the investigation is dynamics involving the cross peaks, slight lineshape distortions from the artifact along the diagonal using medium RF power may not influence the observed dynamics. Although the nonlinear artifact is present in both rephasing and non-rephasing spectra, it is more prominent in the rephasing spectra. We have outlined two approaches to correct for the acousto-optic nonlinearities, which work well if the artifact is solely due to amplitude deviations from the expected diffraction. We discussed an "amplitude correction" scheme, which is based on appropriately scaling the RF power of every streamed pulse sequence to enforce linear pulse-shaper behavior at high RF-power regimes. Such a correction can only be applied in the case where the laser spectrum is stable and the spectral output of the pulse shaper is not distorted by high RF powers. This correction procedure may lead to a decreased signal-to-noise ratio as it requires additional measurements. As a second artifact-correction approach, we showed that the measurement of the integrated intensity of the artifact-contaminated light fields on a photodetector can be used to subtract the artifact contamination in F-2DES. This approach can be implemented through simultaneous measurement of sample fluorescence and the laser intensity but is limited to low artifact-contamination regimes and requires sufficient temporal sampling.

Overall, our results demonstrate that RF and acousto-optic nonlinearities from pulse shapers can result in large spectral responses that obscure the molecular response in multidimensional spectroscopy, as shown here for F-2DES where the pulse shaper is used to generate all four pulses. This effect will also distort coherently detected 2D spectra measured in the collinear geometry with a single AOPDF generating all the required pulses, or in the pump–probe geometry where the AOPDF creates the excitation pulse pair when RF powers outside of the linear regime are used. To take full advantage of AOPDF pulse shapers for implementing multidimensional spectroscopies, care should be taken to either operate within the linear regime of the RF generator, or to account for and correct RF nonlinearities where necessary. When the acousto-optic nonlinearity is corrected, higher RF powers in the nonlinear regime can be used, enabling a larger range of accessible excitation energies. We note that the crystal-dependent diffraction efficiency should be also corrected when an AOPDF shaper is used to create long time delays, as is done here for F-2DES.

Funding. Directorate for Mathematical and Physical Sciences (PHY-1914608); Office of Science (DE-SC0016384); Human Frontier Science Program (LT0056/2024-C); European Research Council (No. 101141366).

Acknowledgments. S.E.S. and J.P.O gratefully acknowledge the support of the National Science Foundation through Grant #PHY-1914608. M.Z. and J.P.O gratefully acknowledge the Office of Basic Energy Sciences, the U.S. Department of Energy Grant DE-SC0016384. J.L. acknowledges support from the HFSP fellowship program under Grant No LT0056/2024-C. T.B. acknowledges funding by the European Research Council (ERC) within Advanced Grant IMPACTS (No. 101141366). We thank Christoph Lambert for providing the dSQAB3 sample, and we thank Nicolas Forget and Luisa Brenneis for helpful discussions.

Disclosures. The authors declare no conflicts of interest.

Data availability. The data that support the findings of this study are openly available in Zenodo [68].

Supplemental document. See Supplement 1 for supporting content.

References

1. D. M. Jonas, "Two-Dimensional Femtosecond Spectroscopy," Annu. Rev. Phys. Chem. **54**(1), 425–463 (2003).
2. S. Biswas, J. Kim, X. Zhang, *et al.*, "Coherent Two-Dimensional and Broadband Electronic Spectroscopies," Chem. Rev. **122**(3), 4257–4321 (2022).
3. E. Fresch, F. V. A. Camargo, Q. Shen, *et al.*, "Two-dimensional electronic spectroscopy," Nat. Rev. Methods Primers **3**(1), 84 (2023).
4. J. D. Hybl, A. W. Albrecht, S. M. Gallagher Faeder, *et al.*, "Two-dimensional electronic spectroscopy," Chem. Phys. Lett. **297**(3-4), 307–313 (1998).
5. M. C. Asplund, M. T. Zanni, R. M. Hochstrasser, *et al.*, "Two-dimensional infrared spectroscopy of peptides by phase-controlled femtosecond vibrational photon echoes," Proc. Natl. Acad. Sci. U.S.A. **97**(15), 8219–8224 (2000).
6. M. Khalil, N. Demirdöven, A. Tokmakoff, *et al.*, "Obtaining Absorptive Line Shapes in Two-Dimensional Infrared Vibrational Correlation Spectra," Phys. Rev. Lett. **90**(4), 047401 (2003).
7. U. Selig, F. Langhojer, F. Dimler, *et al.*, "Inherently phase-stable coherent two-dimensional spectroscopy using only conventional optics," Opt. Lett. **33**(23), 2851–2853 (2008).
8. I. A. Heisler, R. Moca, F. V. A. Camargo, *et al.*, "Two-dimensional electronic spectroscopy based on conventional optics and fast dual chopper data acquisition," Rev. Sci. Instrum. **85**(6), 063103 (2014).
9. V. Volkov, R. Schanz, and P. Hamm, "Active phase stabilization in Fourier-transform two-dimensional infrared spectroscopy," Opt. Lett. **30**(15), 2010–2012 (2005).
10. L. P. DeFlores, R. A. Nicodemus, and A. Tokmakoff, "Two-dimensional Fourier transform spectroscopy in the pump-probe geometry," Opt. Lett. **32**(20), 2966–2968 (2007).
11. M. L. Cowan, J. P. Ogilvie, and R.J.D. Miller, "Two-dimensional spectroscopy using diffractive optics based phased-locked photon echoes," Chem. Phys. Lett. **386**(1-3), 184–189 (2004).
12. T. Brixner, T. Mančal, I. V. Stiopkin, *et al.*, "Phase-stabilized two-dimensional electronic spectroscopy," J. Chem. Phys. **121**(9), 4221–4236 (2004).
13. T. Brixner, I. V. Stiopkin, G. R. Fleming, *et al.*, "Tunable two-dimensional femtosecond spectroscopy," Opt. Lett. **29**(8), 884–886 (2004).
14. J. Réhault, M. Maiuri, A. Oriana, *et al.*, "Two-dimensional electronic spectroscopy with birefringent wedges," Rev. Sci. Instrum. **85**(12), 123107 (2014).
15. W. S. Warren and A. H. Zewail, "Multiple phase-coherent laser pulses in optical spectroscopy. I. The technique and experimental applications," J. Chem. Phys. **78**(5), 2279–2297 (1983).
16. A. M. Weiner, "Femtosecond pulse shaping using spatial light modulators," Rev. Sci. Instrum. **71**(5), 1929–1960 (2000).
17. M. A. Dugan, J. X. Tull, W. S. Warren, *et al.*, "High-resolution acousto-optic shaping of unamplified and amplified femtosecond laser pulses," J. Opt. Soc. Am. B **14**(9), 2348–2358 (1997).
18. F. Verluise, V. Laude, Z. Cheng, *et al.*, "Amplitude and phase control of ultrashort pulses by use of an acousto-optic programmable dispersive filter: pulse compression and shaping," Opt. Lett. **25**(8), 575–577 (2000).
19. S.-H. Shim and M. T. Zanni, "How to turn your pump–probe instrument into a multidimensional spectrometer: 2D IR and Vis spectroscopiesvia pulse shaping," Phys. Chem. Chem. Phys. **11**(5), 748–761 (2009).
20. K. Gundogdu, K. W. Stone, D. B. Turner, *et al.*, "Multidimensional coherent spectroscopy made easy," Chem. Phys. **341**(1-3), 89–94 (2007).
21. J. A. Myers, K. L. Lewis, P. F. Tekavec, *et al.*, "Two-color two-dimensional Fourier transform electronic spectroscopy with a pulse-shaper," Opt. Express **16**(22), 17420 (2008).
22. P. Tyagi, J. I. Saari, B. Walsh, *et al.*, "Two-Color Two-Dimensional Electronic Spectroscopy Using Dual Acousto-Optic Pulse Shapers for Complete Amplitude, Phase, and Polarization Control of Femtosecond Laser Pulses," J. Phys. Chem. A **117**(29), 6264–6269 (2013).
23. J. A. de la Paz, A. Bonvalet, M. Joffre, *et al.*, "Frequency-domain two-dimensional infrared spectroscopy using an acousto-optic programmable dispersive filter," Opt. Express **27**(4), 4140 (2019).
24. K. M. Farrell and M. T. Zanni, "Phase stable, shot-to-shot measurement of third- and fifth-order two-quantum correlation spectra using a pulse shaper in the pump–probe geometry," J. Chem. Phys. **157**(1), 014203 (2022).

25. H.-S. Tan, "Theory and phase-cycling scheme selection principles of collinear phase coherent multi-dimensional optical spectroscopy," J. Chem. Phys. **129**(12), 124501 (2008).
26. P. Hamm and M. Zanni, *Concepts and Methods of 2D Infrared Spectroscopy* (Cambridge University Press: Cambridge, 2011).
27. A. K. De, D. Monahan, J. M. Dawlaty, *et al.*, "Two-dimensional fluorescence-detected coherent spectroscopy with absolute phasing by confocal imaging of a dynamic grating and 27-step phase-cycling," J. Chem. Phys. **140**(19), 194201 (2014).
28. P. Malý, J. Lüttig, S. Mueller, *et al.*, "Coherently and fluorescence-detected two-dimensional electronic spectroscopy: direct comparison on squaraine dimers," Phys. Chem. Chem. Phys. **22**(37), 21222–21237 (2020).
29. S. Draeger, S. Roeding, T. Brixner, *et al.*, "Rapid-scan coherent 2D fluorescence spectroscopy," Opt. Express **25**(4), 3259–3267 (2017).
30. P. F. Tekavec, G. A. Lott, and A. H. Marcus, "Fluorescence-detected two-dimensional electronic coherence spectroscopy by acousto-optic phase modulation," J. Chem. Phys. **127**(21), 214307 (2007).
31. V. Tiwari, Y. A. Matutes, A. T. Gardiner, *et al.*, "Spatially-resolved fluorescence-detected two-dimensional electronic spectroscopy probes varying excitonic structure in photosynthetic bacteria," Nat. Commun. **9**(1), 4219 (2018).
32. G. Nardin, T. M. Autry, K. L. Silverman, *et al.*, "Multidimensional coherent photocurrent spectroscopy of a semiconductor nanostructure," Opt. Express **21**(23), 28617–28627 (2013).
33. A. A. Bakulin, C. Silva, E. Vella, *et al.*, "Ultrafast Spectroscopy with Photocurrent Detection: Watching Excitonic Optoelectronic Systems at Work," J. Phys. Chem. Lett. **7**(2), 250–258 (2016).
34. K. J. Karki, J. R. Widom, J. Seibt, *et al.*, "Coherent two-dimensional photocurrent spectroscopy in a PbS quantum dot photocell," Nat. Commun. **5**(1), 5869 (2014).
35. M. Aeschlimann, T. Brixner, A. Fischer, *et al.*, "Coherent Two-Dimensional Nanoscopy," Science **333**(6050), 1723–1726 (2011).
36. L. Bruder, U. Bangert, M. Binz, *et al.*, "Coherent multidimensional spectroscopy of dilute gas-phase nanosystems," Nat. Commun. **9**(1), 4823 (2018).
37. G. A. Lott, A. Perdomo-Ortiz, J. K. Utterback, *et al.*, "Conformation of self-assembled porphyrin dimers in liposome vesicles by phase-modulation 2D fluorescence spectroscopy," Proc. Natl. Acad. Sci. U.S.A. **108**(40), 16521–16526 (2011).
38. T. Kunsel, V. Tiwari, Y. A. Matutes, *et al.*, "Simulating Fluorescence-Detected Two-Dimensional Electronic Spectroscopy of Multichromophoric Systems," J. Phys. Chem. B **123**(2), 394–406 (2019).
39. P. Tian, D. Keusters, Y. Suzaki, *et al.*, "Femtosecond Phase-Coherent Two-Dimensional Spectroscopy," Science **300**(5625), 1553–1555 (2003).
40. S. E. Sanders, M. Zhang, A. Javed, *et al.*, "Expanding the bandwidth of fluorescence-detected two-dimensional electronic spectroscopy using a broadband continuum probe pulse pair," Opt. Express **32**(6), 8887–8902 (2024).
41. M. López-Ortiz, L. Bolzonello, M. Bruschi, *et al.*, "Photoelectrochemical Two-Dimensional Electronic Spectroscopy (PEC2DES) of Photosystem I: Charge Separation Dynamics Hidden in a Multichromophoric Landscape," ACS Appl. Mater. Interfaces **16**(33), 43451–43461 (2024).
42. L. Bolzonello, F. Bernal-Texca, L. G. Gerling, *et al.*, "Photocurrent-Detected 2D Electronic Spectroscopy Reveals Ultrafast Hole Transfer in Operating PM6/Y6 Organic Solar Cells," J. Phys. Chem. Lett. **12**(16), 3983–3988 (2021).
43. S. Roeding and T. Brixner, "Coherent two-dimensional electronic mass spectrometry," Nat. Commun. **9**(1), 2519 (2018).
44. J. Dostál, F. Fennel, F. Koch, *et al.*, "Direct observation of exciton–exciton interactions," Nat. Commun. **9**(1), 2466 (2018).
45. S. Mueller, J. Lüttig, P. Malý, *et al.*, "Rapid multiple-quantum three-dimensional fluorescence spectroscopy disentangles quantum pathways," Nat. Commun. **10**(1), 4735 (2019).
46. Z. Zhang, K. L. Wells, and H.-S. Tan, "Purely absorptive fifth-order three-dimensional electronic spectroscopy," Opt. Lett. **37**(24), 5058–5060 (2012).
47. B. Kriete, A. S. Bondarenko, R. Alessandri, *et al.*, "Molecular versus Excitonic Disorder in Individual Artificial Light-Harvesting Systems," J. Am. Chem. Soc. **142**(42), 18073–18085 (2020).
48. H. Seiler, S. Palato, and P. Kambhampati, "Coherent multi-dimensional spectroscopy at optical frequencies in a single beam with optical readout," J. Chem. Phys. **147**(9), 094203 (2017).
49. P. Grégoire, A. R. Srimath Kandada, E. Vella, *et al.*, "Incoherent population mixing contributions to phase-modulation two-dimensional coherent excitation spectra," J. Chem. Phys. **147**(11), 114201 (2017).
50. P. Malý and T. Mančal, "Signatures of Exciton Delocalization and Exciton–Exciton Annihilation in Fluorescence-Detected Two-Dimensional Coherent Spectroscopy," J. Phys. Chem. Lett. **9**(19), 5654–5659 (2018).
51. A. A. S. Kalaee, F. Damtie, and K. J. Karki, "Differentiation of True Nonlinear and Incoherent Mixing of Linear Signals in Action-Detected 2D Spectroscopy," J. Phys. Chem. A **123**(19), 4119–4124 (2019).
52. M. Bruschi, L. Bolzonello, F. Gallina, *et al.*, "Unifying Nonlinear Response and Incoherent Mixing in Action-2D Electronic Spectroscopy," J. Phys. Chem. Lett. **14**(30), 6872–6879 (2023).
53. S. Pres, L. Kontschak, M. Hensen, *et al.*, "Coherent 2D electronic spectroscopy with complete characterization of excitation pulses during all scanning steps," Opt. Express **29**(3), 4191–4209 (2021).
54. S. Roeding, "Coherent Multidimensional Spectroscopy in Molecular Beams and Liquids Using Incoherent Observables," (Dissertation, Julius-Maximilians-Universität Würzburg, 2017).

55. S. Mueller and T. Brixner, "Molecular Coherent Three-Quantum Two-Dimensional Fluorescence Spectroscopy," J. Phys. Chem. Lett. **11**(13), 5139–5147 (2020).
56. E. Amarotti, L. Bolzonello, S.-H. Lee, *et al.*, "Photocurrent detected 2D spectroscopy via pulse shaper: insights and strategies for optimally untangling the nonlinear response," arXiv (2025).
57. N. Krebs, R. A. Probst, and E. Riedle, "Sub-20 fs pulses shaped directly in the UV by an acousto-optic programmable dispersive filter," Opt. Express **18**(6), 6164–6171 (2010).
58. A. Galler and T. Feurer, "Pulse shaper assisted short laser pulse characterization," Appl. Phys. B **90**(3-4), 427–430 (2008).
59. A. Monmayrant, S. Weber, and B. Chatel, "A newcomer's guide to ultrashort pulse shaping and characterization," J. Phys. B: At. Mol. Opt. Phys. **43**(10), 103001 (2010).
60. J. Tan, N. Forget, A. Borot, *et al.*, "Dispersion control for temporal contrast optimization," Opt. Express **26**(19), 25003 (2018).
61. M. R. Fetterman, D. Goswami, D. Keusters, *et al.*, "Ultrafast pulse shaping: amplification and characterization," Opt. Express **3**(10), 366–375 (1998).
62. S. S. Mukherjee, D. R. Skoff, C. T. Middleton, *et al.*, "Fully absorptive 3D IR spectroscopy using a dual mid-infrared pulse shaper," J. Chem. Phys. **139**(14), 144205 (2013).
63. P. Tournois, "Acousto-optic programmable dispersive filter for adaptive compensation of group delay time dispersion in laser systems," Opt. Commun. **140**(4-6), 245–249 (1997).
64. S.-H. Shim, D. B. Strasfeld, M. T. Zanni, *et al.*, "Generation and characterization of phase and amplitude shaped femtosecond mid-IR pulses," Opt. Express **14**(26), 13120–13130 (2006).
65. A. Javed, J. Lüttig, K. Charvátová, *et al.*, "Photosynthetic Energy Transfer: Missing in Action (Detected Spectroscopy)?" J. Phys. Chem. Lett. **15**(50), 12376–12386 (2024).
66. K. J. Karki, J. Chen, A. Sakurai, *et al.*, "Before Förster. Initial excitation in photosynthetic light harvesting," Chem. Sci. **10**(34), 7923–7928 (2019).
67. X. Zhao, P. Yu, Y. Luo, *et al.*, "Revealing exciton energy structure and interactions in quantum dots by 25 kHz shot-to-shot phase-cycling 2D electronic spectroscopy," J. Chem. Phys. **163**(11), 114202 (2025).
68. M. Zhang, S. Sanders, J. Lüttig, *et al.*, "Accounting for pulse shaper nonlinearity in action-detected two-dimensional electronic spectroscopy," Zenodo: Version 1.0.4, 17 November 2025, https://doi.org/10.5281/zenodo.17199189.